Optical Engineering

SPIEDigitalLibrary.org/oe

Study on shortwave infrared long-distance imaging performance based on multiband imaging experiments

Lang Junwei
Wang Yueming
Xiao Xizhong
Zhuang Xiaoqiong
Wang Shengwei
Liu Jun
Wang Jianyu

SPIE

Study on shortwave infrared long-distance imaging performance based on multiband imaging experiments

Lang Junwei
Chinese Academy of Sciences
Shanghai Institute of Technical Physics
Room 22711, 500 Yutian Road, Hongkou
Shanghai, 200083, China
and
Graduate University of Chinese Academy of Sciences
Beijing, 100049, China

Wang Yueming
Chinese Academy of Sciences
Shanghai Institute of Technical Physics
Room 22711, 500 Yutian Road, Hongkou
Shanghai, 200083, China

Xiao Xizhong
Chinese Academy of Sciences
Shanghai Institute of Technical Physics
Room 22711, 500 Yutian Road, Hongkou
Shanghai, 200083, China
and
Graduate University of Chinese Academy of Sciences
Beijing, 100049, China

Zhuang Xiaoqiong
Wang Shengwei
Liu Jun
Wang Jianyu
Chinese Academy of Sciences
Shanghai Institute of Technical Physics
Room 22711, 500 Yutian Road, Hongkou
Shanghai, 200083, China
E-mail: jywang@mail.sitp.ac.cn

Abstract. Balloon-borne or ground-based high resolution long range observation has extensive applications in border monitoring and area surveillance. Performance of long-distance oblique or horizontal imaging systems is closely related to the atmospheric transmittance of the observing spectral band. Compared with visible and near infrared, the shortwave infrared (SWIR) band benefits from less scattering effects, which enables it to provide better quality images under harsh atmospheric conditions. We present a signal-to-noise ratio (SNR) model including atmospheric influences. Based on the model, image SNR was calculated in the spectral range of 0.4 μm to 2.5 μm. In order to validate the imaging performance model of SWIR, a multi-band camera was designed and spectral imaging experiments were conducted. The results clearly demonstrated the advantage of SWIR imaging. The experiments show that the contrast and SNR of SWIR images reduced insignificantly for long distances and under low visibility conditions. This advantage makes SWIR multiband cameras suitable for long-distance remote sensing and for observing through haze. [DOI: 10.1117/1.OE.52.4.045008]

Subject terms: imaging system; shortwave infrared; multi-band; multi-spectral imaging; long distance observation; atmospheric transmittance.

Paper 130038 received Jan. 8, 2013; revised manuscript received Mar. 27, 2013; accepted for publication Apr. 2, 2013; published online Apr. 24, 2013.

1 Introduction

Shortwave infrared (SWIR) remote sensing is widely used in earth observation and mineral exploration. Its imaging principle is similar to that of visible and near infrared (VNIR), which responds primarily to reflected light from objects.[1] In this paper, SWIR is defined as the wavelength range of 1.1 μm to 2.5 μm,[2] a range with decent atmospheric transmittance because of reduced scattering effects. On account of this property, many institutions started to research SWIR imaging performance, such as the US Army,[3] the US Navy,[4] Goodrich Corp.,[5,6] Litton Itek Optics,[2] Sarnoff,[7] Raytheon,[8] and Carl Zeiss.[9] The results showed that the image quality of SWIR is significantly higher than that of VNIR (0.4 μm to 1.1 μm) at long distance and under low visibility conditions; that is to say, SWIR could realize a longer observation range. This advantage makes SWIR imagers suitable for balloon-borne or ground-based high resolution long-range imaging, which has extensive applications in border monitoring and area surveillance.

For long-distance oblique or horizontal imaging, the light signal needs to pass through dense air in the bottom layer of the atmosphere. Therefore the imaging quality relies on atmospheric transmittance to a great extent. In previous research,[1–9] the transmittance difference between VNIR and SWIR bands were generally discussed and the experiments involving panchromatic imaging at long distance or under hazy weather condition were discussed. In this paper, atmospheric influences were added to the calculation of image quality, and an signal-to-noise ratio (SNR) model of VNIR and SWIR, including atmospheric influences, is presented. Combined with optical parameters, the image SNR and the contrast between the background and the objects are specifically quantified. Furthermore, in order to compare imaging performances of different wavelengths through the long distances in bottom layer atmospheres, spectral imaging experiments were conducted. The results clearly showed the changing process of image quality from 0.4 μm to 2.5 μm, and supported the previous reports.

2 Atmospheric Transmittance Analysis

2.1 *Atmospheric Optical Characteristics*

The energy obtained by the remote sensing instruments generally includes reflected light from the objects, atmospheric scattering, and thermal radiance from objects and path radiance. In SWIR and VNIR imaging systems, thermal radiance is negligible. The primary atmospheric optical phenomenon that affects imaging performance is scattering. Table 1 shows some typical air particles and their scattering processes.[10,11] Rayleigh scattering caused by air molecules, small aerosols and haze particles is inversely proportional to the fourth power of wavelength and Mie scattering also increases as the wavelength decreases.[12,13] In the case of rain or heavy fog, the scale of air particles is much larger than that of SWIR and VNIR wavelengths, thus both wavebands are seriously affected by geometrical scattering. As a result, SWIR advantages over VNIR are particularly observable under sunny, hazy and misty weather conditions.

As the photon detectors used in VNIR and SWIR bands have identical optical parameters, signal response is decided by the number of photons obtained by the imagers. Spectral radiance at the entrance pupil of the instrument, as well as proportions of every energy component, could be calculated by MODTRAN.[14] Figure 1 shows the calculation results of a typical situation with 30-deg.solar elevation angle, 0.3 albedo, mid-latitude summer with rural aerosol model and 23 km visibility. The unit has been converted from $W \cdot cm^{-2} \cdot Sr^{-1} \cdot \mu m^{-1}$ to photons $\cdot s^{-1} \cdot cm^{-2} \cdot Sr^{-1} \cdot \mu m^{-1}$ according to Planck's law.

Table 1 Typical scattering particles.

Particle type	Radius (μm)	Scattering process
Air molecules	10^{-4}	Rayleigh
Haze	10^{-2}-1	Rayleigh-Mie
Fog	1-20	Mie-Geometrical
Rain	10^{2}-10^{4}	Geometrical

Figure 1(a) and 1(b) illustrate the spectral photon radiance at the entrance pupil with different observation distances. The red curve represents the spectral photon radiance of reflected light from objects and the green curve represents the total spectral photon radiance including signal from objects, atmospheric scattering and a small amount of thermal radiance.

2.2 *SNR Model and Imaging Performance Analysis*

Assuming that within an integration period, the number of electrons generated by photo-electronic conversion of each pixel is n_{total}, then[15,16]

$$n_{\text{total}} = \frac{\pi A_d}{4F^2} \cdot T_{\text{int}} \int_{\lambda_1}^{\lambda_2} N_{\lambda\text{photon}} \cdot \tau_\lambda \cdot \eta_\lambda d\lambda, \tag{1}$$

where N_{photon} is the spectral photon radiance at the entrance pupil; A_d is pixel area; $1/F$ is system relative aperture; T_{int} is integration time; τ is system optical efficiency; and η is the quantum efficiency of the detector. To the VNIR and SWIR bands, energy obtained by the instrument is primarily composed of objects' reflected light and atmosphere scattering. The number of electrons generated by photo-electronic conversion could be expressed as

$$n_{\text{total}} = n_{\text{signal}} + n_{\text{scatter}},$$

where n_{signal} represents the number of electrons generated by objects' signal light, while n_{scatter} is the number of electrons generated by atmospheric scattering. The SNR of the image acquired by the instrument is shown as Eq. (2):[17,18]

$$\text{SNR} = \frac{n_{\text{signal}}}{n_{\text{noise}}} = \frac{n_{\text{signal}}}{\sqrt{n_{\text{total}} + n_{\text{nread}}^2}} = \frac{n_{\text{signal}}}{\sqrt{n_{\text{signal}} + n_{\text{scatter}} + n_{\text{nread}}^2}}. \tag{2}$$

The total number of noise electrons is represented as n_{noise}, which includes two parts: shot noise $\sqrt{n_{\text{total}}}$, and

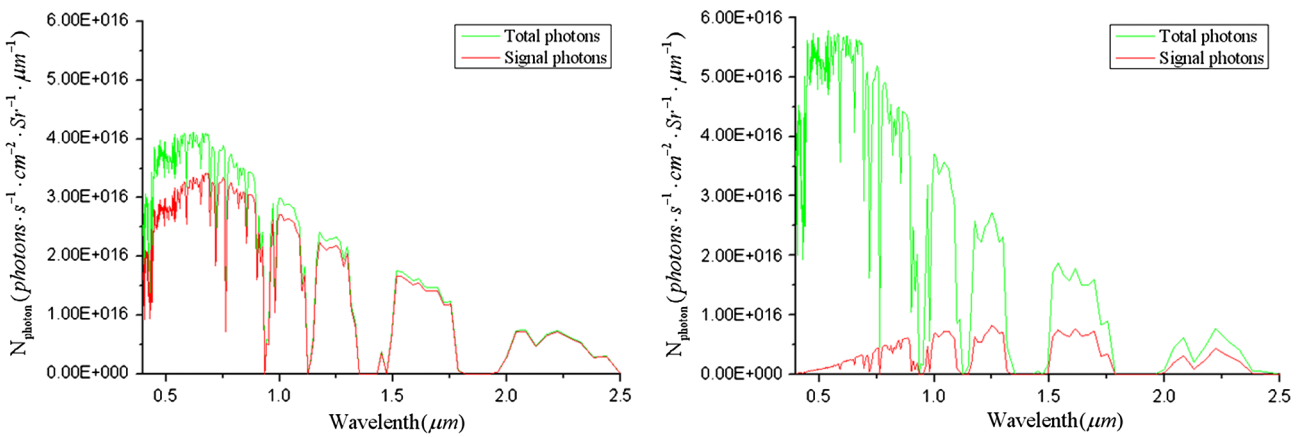

(a) Observation distance: 1km **(b) Observation distance: 20km**

Fig. 1 Spectral photon radiance at the entrance pupil. (a) Observation distance: 1 km, (b) observation distance: 20 km.

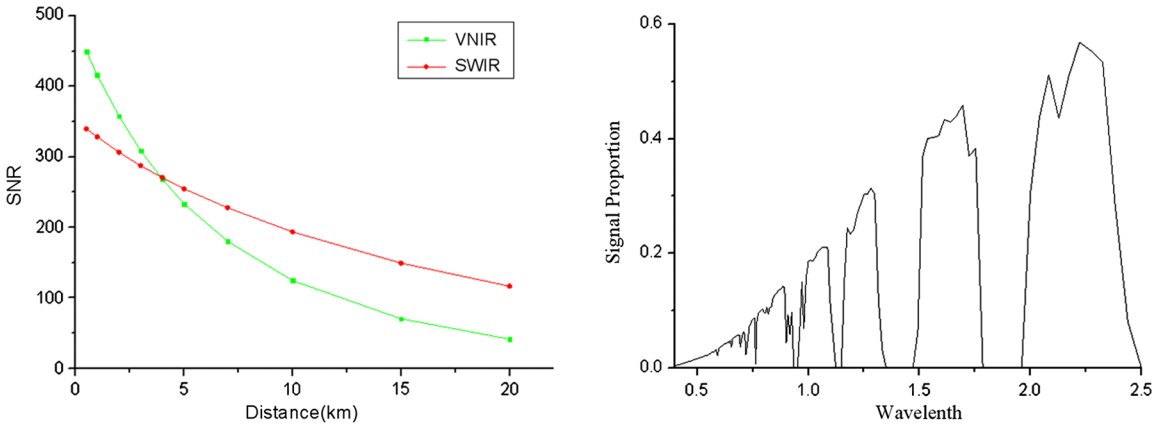

(a) Visibility 23km, observation distance from 1km to 20km (b) Visibility 23km, observation distance 20km

Fig. 2 SNR and the proportion of valid signal of VINR and SWIR images at different observation distance. (a) Visibility 23 km, observation distance from 1 km to 20 km, (b) visibility 23 km, observation distance 20 km.

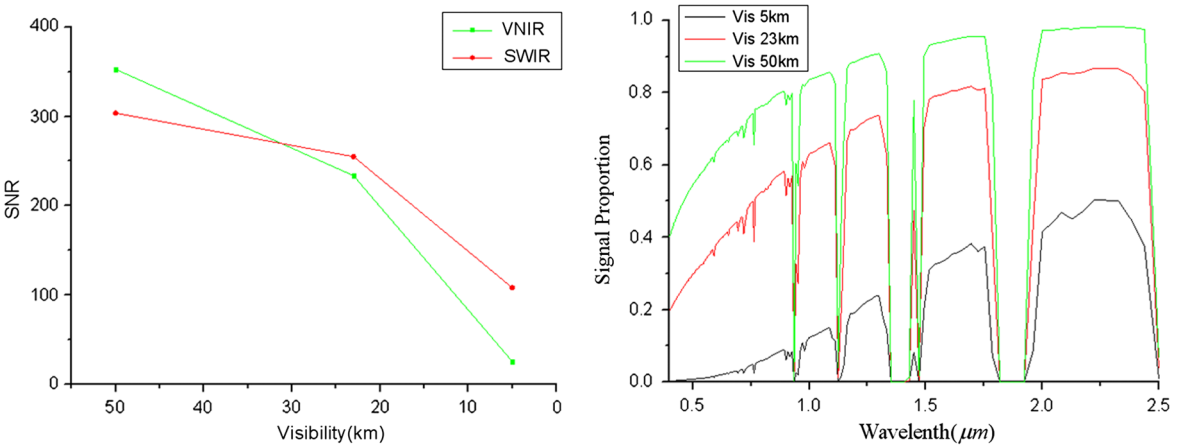

(a) SNR (b) Signal proportion

Fig. 3 SNR and the proportion of valid signal of VNIR and SWIR images at different visibilities at 5 km. (a) SNR, (b) signal proportion.

readout noise of detector and electronics n_{nread}. Figure 2 shows that the signal attenuation of VNIR is not significant in short distance observations, and the number of valid signal photons obtained by the instrument is larger than that of SWIR. However, in long distance observations, the valid signal of VNIR attenuates severely because of atmospheric scattering and results in a very small n_{signal}. On the other hand, n_{scatter} is quite large because the instrument captures a great amount of background scattered light. This part of energy occupies a large proportion of the instrument's dynamic range and hence superimposes the valid signal over a large background scattering signal. Consequently, the valid signal is easy to be drowned out, and the contrast between objects and background is reduced. Meanwhile, this part of energy also significantly increases $\sqrt{n_{\text{total}}}$, the shot noise, and decreases the image SNR. SWIR, however, is not very sensitive to atmospheric scattering. As a result, signal attenuation and the energy increase of scattered light are remarkably lower than those for VNIR bands as the observation distance grows, and the image SNR also reduces more slowly.

It is assumed that the system parameters of VNIR and SWIR imagers are the same (F number is 16, pixel size is 30 μm × 30 μm, quantum efficiency is 60%, optical efficiency is 70%, integration time is 1 ms, and total readout noise of detector and electronics is 100 electrons). With the simulation of MODTRAN and the calculation in accordance with Eqs. (1) and (2), the theoretical SNR of SWIR and VNIR images could be quantified as shown in Fig. 2.

The green curve in Fig. 2(a) represents SNR of VNIR bands (0.4 μm to 1.1 μm), while the red curve represents that of SWIR (1.1 μm to 2.5 μm). In the case of high visibility (23 km) and short observation distance, the SNR of VNIR bands is higher than that of SWIR bands due to more sunlight energy and limited energy loss. As observation distance increases, the SNR of VNIR bands reduces rapidly due to scattering effects, while SWIR benefits from less scattering effects. Due to the relatively weak attenuation of both the background and the target signals, the SWIR SNR is significantly higher than that of the VNIR bands. Figure 2(b) shows the proportion of valid signal photons to total photons

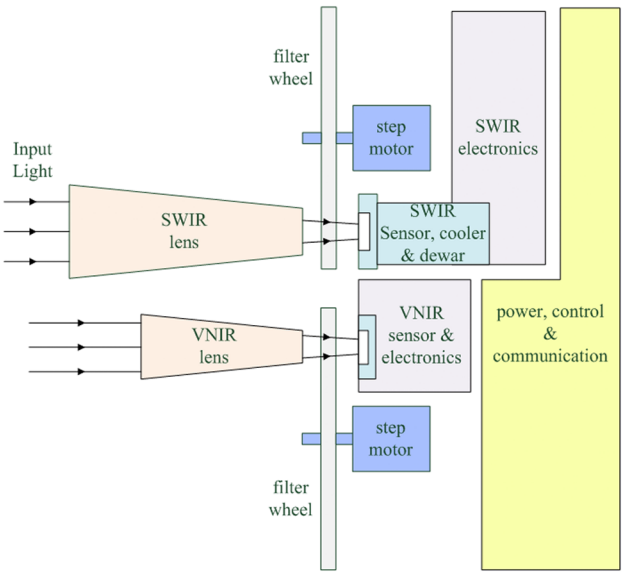

Fig. 4 Schematic of the multiband imager.

Table 2 Instrument parameters.

	VNIR camera	SWIR camera
Dimension	300 mm × 400 mm × 500 mm (lenses not included)	
Weight	28 kg	
Detector	512 × 512 CMOS	500 × 256 MCT
IFOV	0.15 mrad	0.1 mrad
Focal length	250 mm	300 mm
Bandwidth	80 nm, PAN: 400–1000 nm	70 nm, PAN: 900–2500 nm
Central wavelength	450 nm, 550 nm, 650 nm 750 nm, 850 nm, PAN	1292 nm, 1570 nm, 1695 nm, 2140 nm, 2266 nm, PAN
Quantization bits	14 bit	

count from 20 km observation distance and 23 km visibility. The curve indicates that signal of SWIR bands accounts for a much greater proportion in the total energy than that of VNIR bands; that is to say, SWIR images have a higher contrast between objects and background. As seen from the above analysis, SWIR long distance imaging performance is superior to VNIR bands.

Figure 3(a) illustrates the relationship between image SNR and visibility at a certain observing distance (5 km). With the high energy of sunlight and the limited scattering effect at excellent visibility, high quality images could be obtained by VNIR imagers. When visibility decreases, the SNR and the contrast of VNIR images attenuate rapidly as atmospheric scattering increases. Nevertheless, the SNR of SWIR images reduces relatively slowly, and becomes higher than the SNR of VNIR bands as visibility decreases. It follows that the proportion of valid signal is also larger, as shown in Fig. 3(b). In conclusion, SWIR bands are not as heavily dependent on atmospheric conditions as VNIR bands and are capable of observing though haze.

3 Instrument Structure and Imaging Experiments

In order to verify the analysis of atmospheric transmittance and imaging performance described previously, a multiband imager was designed and built, comprising a SWIR multi-band camera and a VNIR multi-band camera. Its comprehensive imaging performance can be assessed from the color images from this multispectral imager.

3.1 *Design of the Multiband Imager*

The instrument is composed of lenses, filter wheels, detectors and electronics, as shown in Fig. 4. The filter wheels are placed between lenses and detectors and their rotation is driven by step-motors in order to select the shooting band.

There are six bands for each camera. The VNIR camera has RGB bands, two near-infrared bands and a panchromatic channel; The SWIR camera is set five bands and a panchromatic channel. Table 2 shows the specific parameters of the instrument.[19,20]

The structure of the instrument is shown in Fig. 5.

This camera is able to observe targets in both VNIR and SWIR bands, and the co-registration of the two sensors is

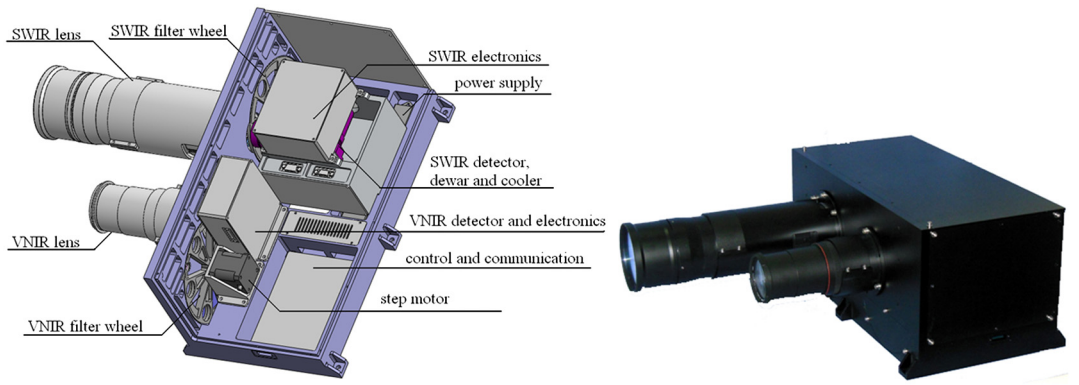

(a) Instrument structure **(b) Instrument picture**

Fig. 5 The instrument design and its picture. (a) Instrument structure, (b) instrument picture.

achieved by post image processing (Visual C++, Origin and Photoshop software).

3.2 *Imaging Experiments and Results*

Two groups of experiments were designed in order to verify SWIR imaging performance:

1. An imaging experiment at a short distance and low visibility, which is used to validate SWIR imaging performance though light haze.
2. An imaging experiment at a long distance and high visibility, which is used to validate SWIR imaging performance at long distances.

3.2.1 *Imaging experiment at a short distance and low visibility*

The imaging weather conditions were light haze with meteorological visibility less than 5 km. The two target buildings were respectively 3.5 km and 4.5 km distant from the observation point, as shown in Fig. 6.

Figure 7(a) is a true color visible image and Fig. 7(b) is a SWIR pseudo-color image of the scene. The visible image

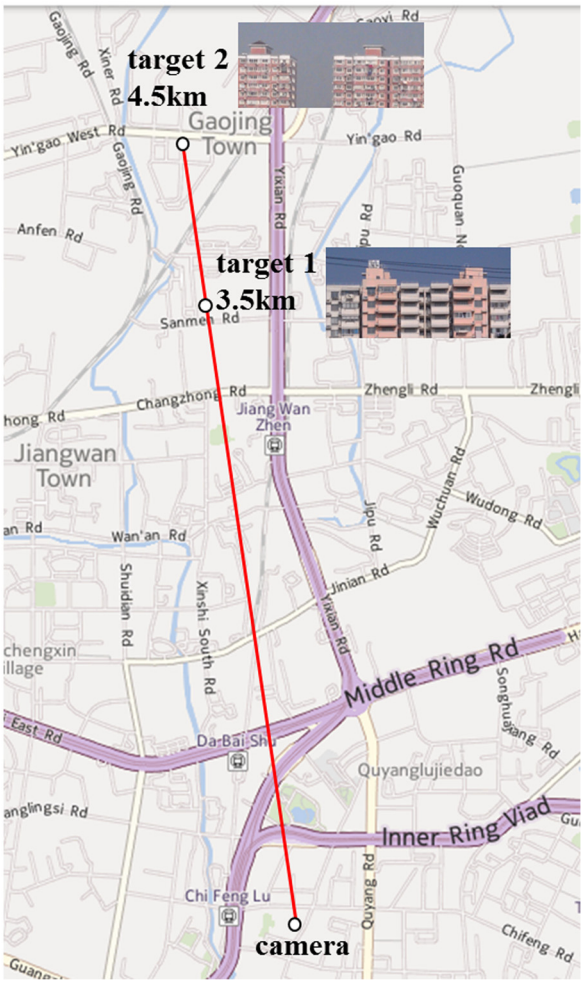

Fig. 6 Schematic of experiment 1.

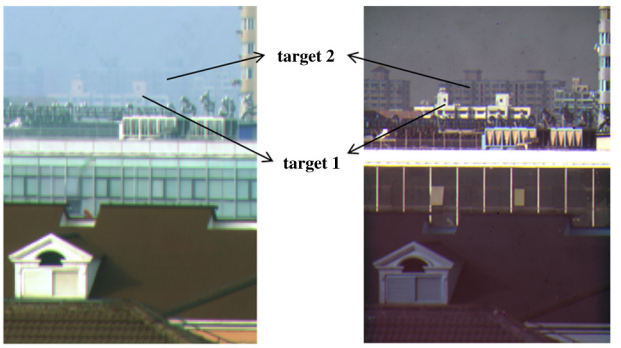

(a) R650nm G550nm B450nm **(b) R2140nm G1695nm B1292nm**

Fig. 7 Fused color images of experiment 1. (a) R650 nm G550 nm B450 nm, (b) R2140 nm G1695 nm B1292 nm.

displays the broad contours of target 1, but target 2 is almost drowned in the sky background and difficult to distinguish. In contrast, both target 1 and target 2 are clearly shown by the SWIR image, and the contrast between the targets and the sky background is evident.

The quality difference between each observation from short to long wavelength could be readily seen as shown in Fig. 8. In the image at 450 nm, the sky background is very bright, and targets 1 and 2 are indistinguishable from the sky radiation. At the near-infrared band of 750 nm, target 1 is just visible, but the outline of target 2 is barely visible. In SWIR bands, however, targets 1 and 2 can be seen clearly.

The VNIR and SWIR images are co-registered as shown in Fig. 9(a). In Fig. 9(b), the corresponding original pixels of selected bands from the VNIR and SWIR sensors over the same geographical area are extracted. Figure 10 shows the profiles of these pixels. The contrast between the targets and the backgrounds is clearly seen in the profiles. The targets are concrete buildings, and albedo of concrete materials has no significant difference between VNIR and SWIR bands,[21] so the contrast between VNIR and SWIR images is mainly due to atmospheric scattering phenomenology.

3.2.2 *Imaging experiment at a long distance and high visibility*

The imaging weather conditions were sunny with meteorological visibility more than 15 km. The target building was the Shanghai World Financial Center, which is 13 km distant from the observation point, as shown in Fig. 11.

Figure 12(a) is a true color visible image and Fig. 12(b) is a SWIR pseudo-color image. The buildings close to the camera in the two images are clear, but in the SWIR image the contrast between the sky background and the target building is more apparent. In addition, most distant clouds in the VNIR image are submerged in the background, and only a small amount of bright clouds could be distinguished. In contrast, the SWIR image shows abundant clouds in the sky.

Figure 13 shows that in the image at 450 nm, the sky background is bright, which makes the target very vague. In the near-infrared band of 750 nm, the target building is

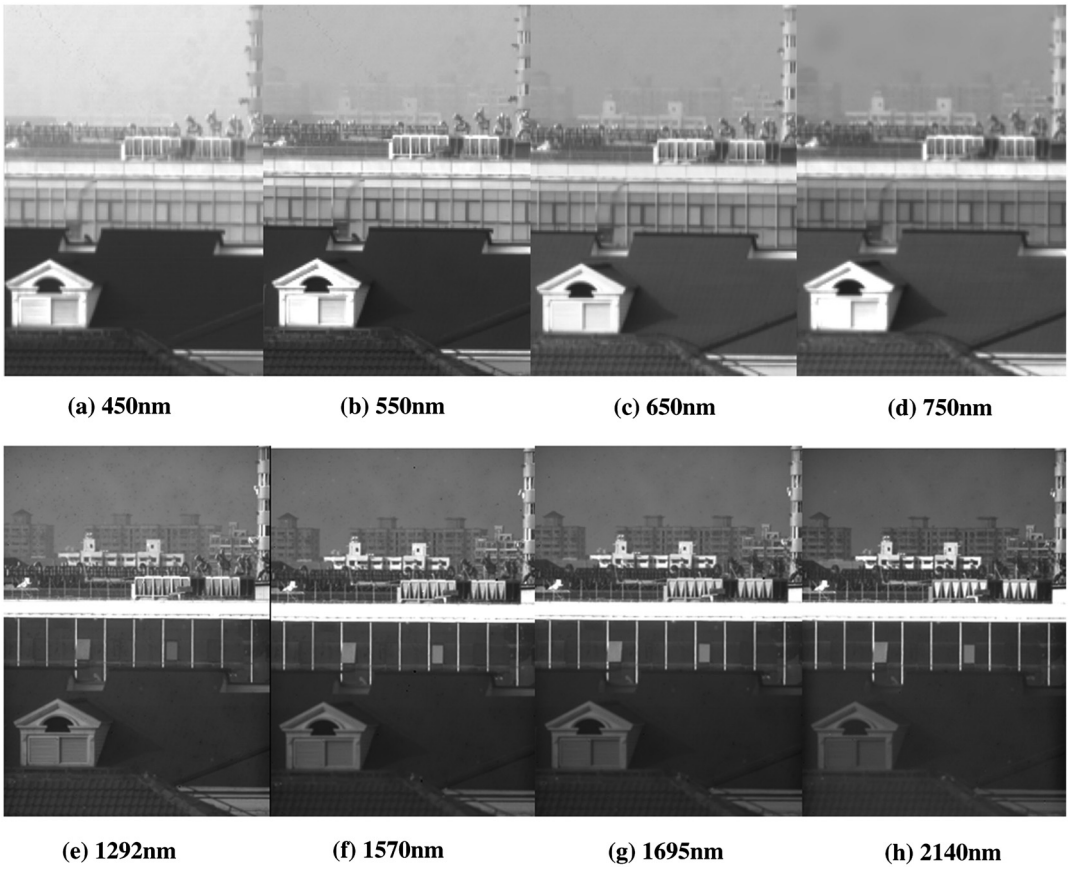

Fig. 8 The images of different wavelengths in experiment 1. (a) 450 nm, (b) 550 nm, (c) 650 nm, (d) 750 nm, (e) 1292 nm, (f) 1570 nm, (g) 1695 nm, and (h) 2140 nm.

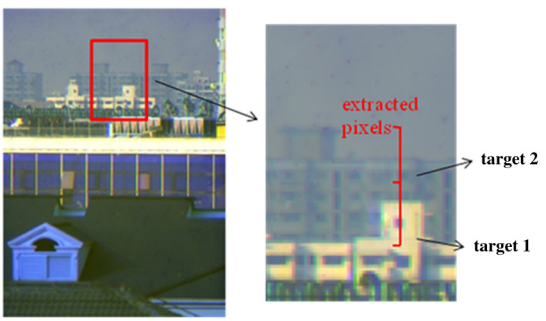

(a) Co-registered image (R 1695nm G1292nm B 650nm) and extracted area

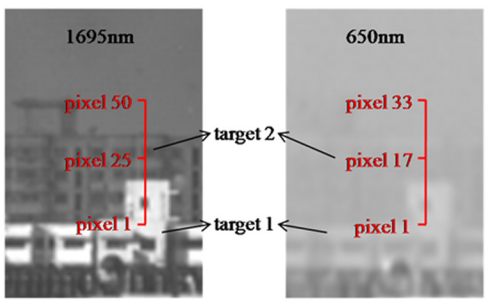

(b) Extracted pixels of each original image

Fig. 9 The location of the profile of extracted pixels in each image in experiment 1. (a) Co-registered image (R1695 nm G1292 nm B650 nm) and extracted area, (b) extracted pixels of each original image.

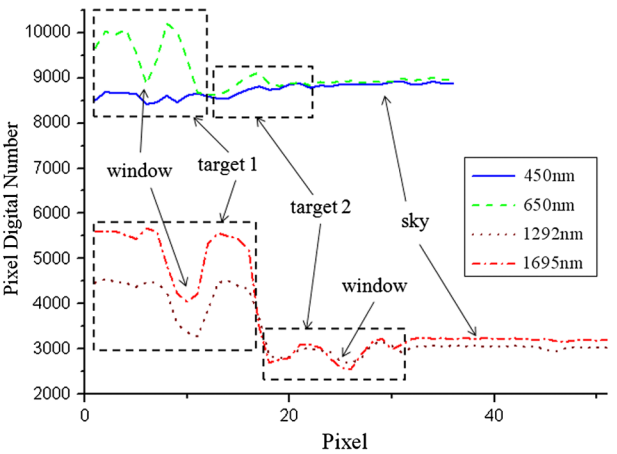

Fig. 10 The DN curves of extracted pixels in experiment 1.

clearly visible and clouds also start to emerge. With the longer wavelengths, the clouds start to appear clearer.

As before, a common profile of pixels is extracted and analyzed from each image, as shown in Figs. 14 and 15.

In the 450 nm image, the fluctuation of DN curve is insignificant and all the clouds are drowned in the sky background; at 650 nm, the sky background is still bright but some near and thick clouds are becoming distinguishable.

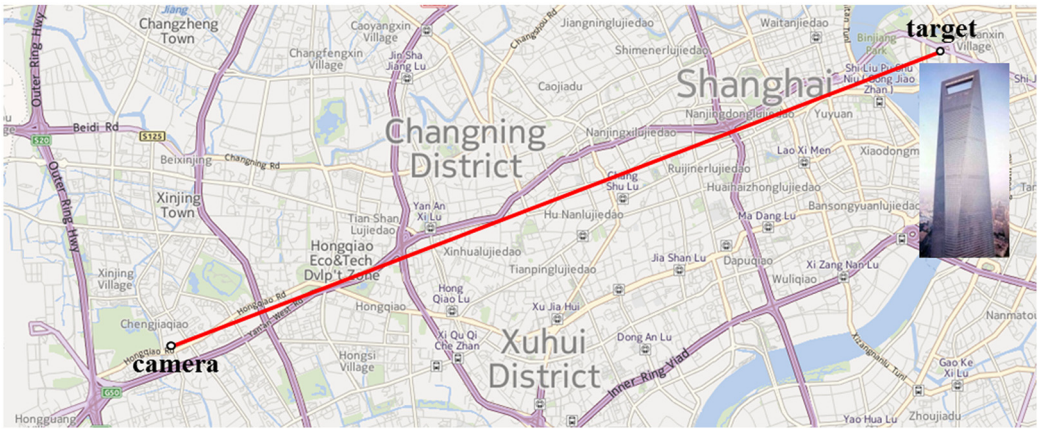

Fig. 11 Schematic of experiment 2.

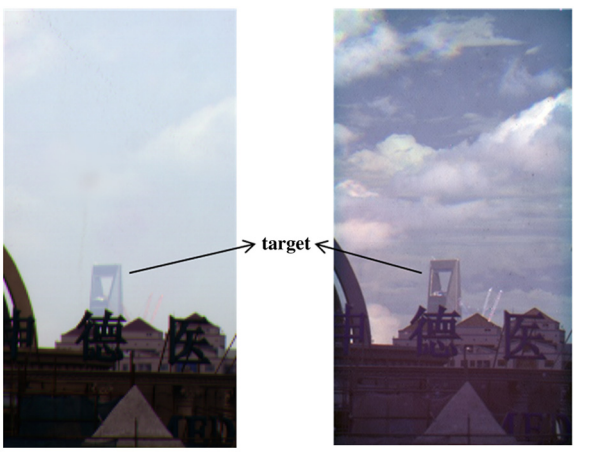

(a) R650nm G550nm B450nm (b) R2140nm G1695nm B1292nm

Fig. 12 Fused color images of experiment 2. (a) R650 nm G550 nm B450 nm, (b) R2140 nm G1695 nm B1292 nm.

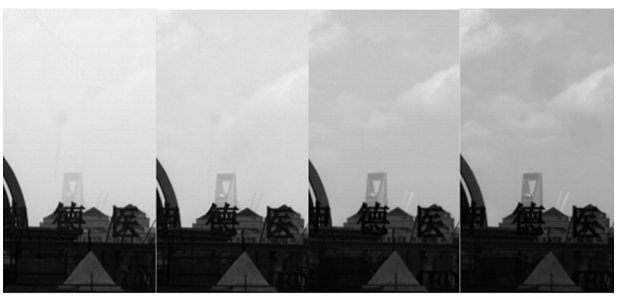

(a) 450nm (b) 550nm (c) 650nm (d) 750nm

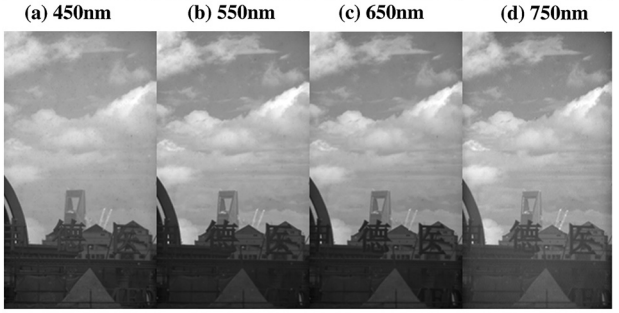

(e) 1292nm (f) 1570nm (g) 1695nm (h) 2140nm

Fig. 13 The images of different wavelengths in experiment 2. (a) 450 nm, (b) 550 nm, (c) 650 nm, (d) 750 nm, (e) 1292 nm, (f) 1570 nm, (g) 1695 nm, (h) 2140 nm.

(a) Co-registered image (R 1695nm G1292nm B 650 nm) and extracted area

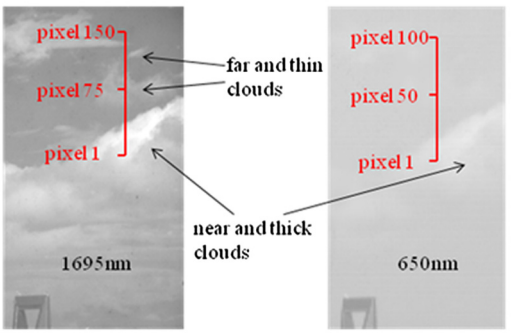

(b) Extracted pixels of each original image

Fig. 14 The location of the profile of extracted pixels in each image in experiment 2. (a) Co-registered image (R1695 nm G1292 nm B650 nm) and extracted area, (b) extracted pixels of each original image.

In SWIR images, the background is evidently darker and the contrast between the reflected lights from the clouds and the sky background is stronger. Far and thin clouds can also be distinguished in the SWIR images. The sizes of cloud particles are similar to that of fog, and thick clouds are composed of densely packed particles of radius of more than 10 μm. The scattering process of these kinds of particles in VNIR and SWIR bands is substantially the same, so the response of clouds remains similar in both wavebands.[10,12]

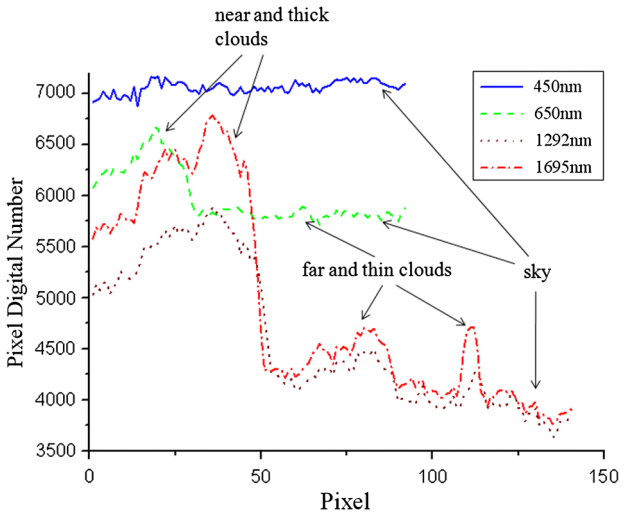

Fig. 15 DN curve of extracted pixels in experiment 2.

4 Summary

In remote sensing, especially in long-range oblique or horizontal observation, imaging quality is closely related to atmospheric transmittance.

The atmospheric simulation and the SNR calculations show that the influence of atmospheric scattering on SWIR imaging performance is much less than that on VNIR bands. As the observation distance grows or the visibility reduces, the SNR and the signal proportion of SWIR images attenuate relatively slowly. That is, at long observation distances or under low visibility conditions, imaging performance of SWIR is significantly higher than that of VNIR bands.

For this study, a multiband camera including VNIR and SWIR bands was built and using it, two experiments were conducted under different weather conditions. The multispectral images have verified the SWIR imaging performance predicted through modelling and confirmed that these bands are suitable for observing through haze and for long distance remote sensing.

This study can be applied to ground-based or balloon-borne long-range high resolution imaging, which have extensive applications in border monitoring, area surveillance and search and rescue.

References

1. M. P. Hansen and D. S. Malchow, "Overview of SWIR detectors, cameras, and applications," *Proc. SPIE* **6939**, 69390I (2008).
2. R. N. Lane, "The SWIR advantage," *Proc. SPIE* **2555**, 246–254 (1995).
3. M. Norton, "Short-wave (1-2.8 μm) imagery for fun and profit," *Proc. SPIE* **2933**, 9–31 (1996).
4. K. P. Judd, J. R. Waterman, and J. M. Nichols, "Passive shortwave infrared technology and hyperspectral imaging for maritime applications," *Proc. SPIE* **7660**, 766008 (2010).
5. D. Malchow, "High speed short wave infrared (SWIR) imaging and range gating," *Proc. SPIE* **6541**, 654106 (2007).
6. Sensors Unlimited Inc., "The advantages of SWIR imaging," http://www.sensorsinc.com (2013).
7. J. Ng, M. Piacentino, and B. Caldwell, "Overcoming adverse weather conditions with a common optical path, multiple sensors and intelligent image fusion system," *Proc. SPIE* **6946**, 694605 (2008).
8. M. MacDougal et al., "InGaAs focal plan arrays for low light level SWIR imaging," *Proc. SPIE* **8012**, 801221 (2011).
9. M. G. Gerken et al., "Shortwave infrared camera with extended spectral sensitivity," *Proc. SPIE* **8353**, 838304 (2012).
10. Z. Ghassemlooy, W. Popoola, and S. Rajhbandari, *Optical Wireless Communications: System and Channel Modeling*, p. 109, CRC Press, Boca Raton, Florida (2012).
11. C. M. Payne, *Principles of Naval Weapon Systems*, p. 122, Naval Institute Press, Annapolis, Maryland (2006).
12. E. J. McCartney, "Scattering by molecules and particles," in *Optics of the Atmosphere*, pp. 177–178, John Wiley & Sons, Inc., New York (1976).
13. F. G. Smith, "Atmospheric propagation of radiation," in *The Infrared and Electro-Optical Systems Handbook*, J. S. Accetta and D. L. Shumaker, Eds., pp. 92–119, Infrared Information Analysis Center (MI) & SPIE Optical Engineering Press, Bellingham, WA (1993).
14. Ontar Corp., *PcModWin Manual*, Ontar Corp, MA (June 2001).
15. S. B. Campana, "Passive electro-optical systems," in *The Infrared and Electro-Optical Systems Handbook*, J. S. Accetta and D. L. Shumaker, Eds., pp. 130–131, Infrared Information Analysis Center (MI) & SPIE Optical Engineering Press, Bellingham, WA (1993).
16. J. Y. Wang, Y. M. Wang, and C. L. Li, "Noise model of hyperspectral imaging system and influence on radiation sensitivity," *J. Remote Sens.* **14**(4), 607–620 (2010).
17. A. Eckardt et al., "SNR estimation for advanced hyperspectral space instrument," *Proc. SPIE* **5883**, 588303 (2005).
18. Y. M. Wang et al., "Application of advanced IR-FPA in high-sensitivity pushbroom SWIR hyper-spectral imager," *Proc. SPIE* **8353**, 83532V (2012).
19. Sofradir Corp., "NEPTURE-SW 500×256 HgCdTe(30 um pitch) a large and high performance detector," http://www.sofradir.com (2008).
20. Optec Corp., "LENS OB-SWIR300/3.5-P/N C0245," http://www.optec.eu (4 September 2009).
21. S. Bhaskaran, B. Forster, and T. Neal, "Integrating airborne hyperspectral sensor data with GIS or hail storm post-disaster management," in *22nd Asian Conf. on Remote Sensing*, Vol. 1, pp. 765–770, Centre for Remote Imaging, Sensing and Processing; National University of Singapore; Singapore Institute of Surveyors and Valuers; Asian Association of Remote Sensing, Singapore (2001).

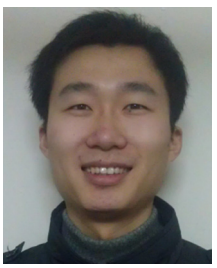

Lang Junwei is currently a PhD candidate at the Shanghai Institute of Technical Physics, Chinese Academy of Sciences. His research interests include imaging system design, hyperspectral imaging technologies, remote sensing instrument and sensor application. He received his BS degree in electronic engineering from East China Normal University in 2009.

Wang Yueming is currently a project manager at Shanghai Institute of Technical Physics. He has responsibility for R&D of high performance short-wave infrared imaging systems. His research interests include the system design and simulation of infrared and hyperspectral imaging system. He received his BS degree in mechanical engineering at Tsinghua University in 2000, and his PhD in electronic science and technology from the Graduate School of Chinese Academy of Sciences in 2005.

Xiao Xizhong is currently a PhD candidate at the Shanghai Institute of Technical Physics, Chinese Academy of Sciences. He received his BS degree in electronic engineering from Fudan University in 2010. His research interests include infrared imaging system design and infrared target analysis.

Zhuang Xiaoqiong is currently an electronic engineer at Shanghai Institute of Technical Physics. She received her BS degree and MS degree in electronic engineering from Nanjing Normal University in 2004 and 2007. Her research interests include short-wave infrared system design and high-speed data acquisition.

Wang Shengwei is currently an electronic engineer at Shanghai Institute of Technical Physics. He received his BS degree in electronic engineering from University of Shanghai for Science & Technology in 2006. His research interests include pointing mirror control and remote communication.

Liu Jun is currently a mechanical engineer at Shanghai Institute of Technical Physics. He received his BS degree in mechanical engineering from North University of China and MS degree in mechanical engineering from Xidian University. His research interests include mechanical design and analysis of space-borne optoelectronic system.

Wang Jianyu is currently the research professor of Shanghai Institute of Technical Physics, Chinese Academy of Sciences. He is the vice chairman of Chinese Society of Space Research, and the director of Chinese Optical Society. He is an associate editor of *Journal of Infrared and Millimeter Wave* and *Journal of Applied Science*. His research interests include passive and active optoelectronic remote sensing system, space quantum communication technologies, infrared optics and data processing. He received his BS degree in physics from Hangzhou University, and his MS degree and PhD from Shanghai Institute of Technical Physics, Chinese Academy of Sciences.